coatings

MDPI

Article

Rolled Waterproofing Coating Delamination Detection by High-Voltage Testing

Vladimir Syasko [1], Alexey Musikhin [2], Igor Gnivush [3,*], Maria Stepanova [1] and Anna Vinogradova [3]

[1] D.I. Mendeleev Institute for Metrology (VNIIM), Moskovsky Ave, 19, 190005 St. Petersburg, Russia; 9334343@gmail.com (V.S.)
[2] LLC "KONSTANTA", Ogorodny Lane, 21, 198095 St. Petersburg, Russia; musihinaleksei@mail.ru
[3] Faculty of Mechanical Engineering, Empress Catherine II Saint Petersburg Mining University, 21st Line, 2, 199106 St. Petersburg, Russia; vinogradova_aa@pers.spmi.ru
* Correspondence: klin4_g@mail.ru; Tel.: +7-981-794-28-80

Abstract

This study assesses the possibility of identifying non-through defects in dielectric coatings, specifically interfacial defects located at the metal–coating boundary, by means of high-voltage non-destructive testing. It is demonstrated that partial discharges causing characteristic distortions of the applied test-voltage pulse can be used as a reliable diagnostic feature of such defects. Using an equivalent capacitive representation of a defective coating, a relationship is established between the apparent charge and the geometry of the air-filled gap. The proposed approach is supported by COMSOL simulations of the electric-field distribution and by experiments performed on Plexiglas specimens containing blind holes of different depths. In addition, a method is developed for isolating the partial-discharge signal based on a weighted sum of increments in the root-mean-square deviations of the second derivative of the voltage waveform. The resulting relationships enable estimation of the residual coating thickness in the defect region.

Keywords: holiday detection; coating defect; dielectric coatings; partial discharges; interfacial defect at the metal–coating interface (interfacial defect)

1. Introduction

High-voltage testing is a high-throughput non-destructive technique for evaluating the continuity of dielectric coatings on metal structures; it relies on generating a high-intensity electric field in the inspection zone, which produces spark discharges at coating holidays [1–3]. This approach allows coating defects that impair the insulating performance to be revealed [4–6].

Currently, the high-voltage method is widely applied to detect through defects such as pores and micropores, channels, cracks, and cavities [7–9]. In industrial protective coatings, however, defects of a different nature can arise both during application and in service—including blisters, coating–substrate delamination, foreign inclusions, interlayer separation, and craters—which are not through defects [10–12]. With time, these imperfections may promote coating degradation, ultimately resulting in through defects and shortening the service life of the protected component [13–15]. Such defects are frequently encountered at joints between sheets of waterproofing materials in roofing systems, leading to a gradual loss of coating performance. Meanwhile, conventional high-voltage testing procedures [16–18] are unable to detect non-through defects because no continuous channel exists in the coating to sustain a detectable spark discharge.

Check for updates

Academic Editor: Chang-Hwan Choi

Received: 15 April 2026
Revised: 19 May 2026
Accepted: 24 May 2026
Published: 26 May 2026

Copyright: © 2026 by the authors. Licensee MDPI, Basel, Switzerland. This article is an open access article distributed under the terms and conditions of the Creative Commons Attribution (CC BY) license.

A number of studies on high-voltage testing for assessing the continuity of dielectric coatings focus on detecting through defects, for which a full spark discharge serves as the informative feature. Partial discharges in gas cavities and at dielectric interfaces, as well as the relationship between apparent charge and defect geometry, have also been investigated separately. However, these findings have not been applied to the diagnosis of non-through hidden defects—internal cavities and interfacial delamination at the metal–coating interface. In practical procedures, partial discharges are typically treated as interference, and estimation of the delamination height from distortions of the test-voltage pulse has not been addressed. In addition, high-voltage approaches for thin-spot regions rely on breakdown with the formation of a through channel, which requires subsequent coating repair. This substantiates the need for a non-destructive approach that exploits partial discharges and establishes a quantitative relationship between the measured parameters and defect geometry.

2. Materials and Methods

Non-through coating defects can be classified into unacceptable thin spots, internal inclusions [19,20], and interfacial defects [21–23]. Since the aim of this study is associated with analyzing discharge processes in a defect at the metal–coating interface, only interfacial defects are considered below.

Interfacial defects are formed when the coating delaminates from the metal substrate and are characterized by the delamination height d_1 from the substrate (Figure 1).

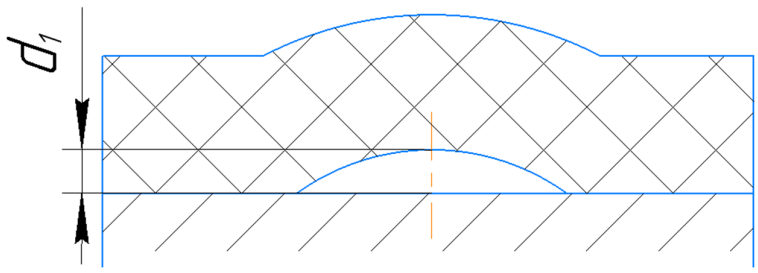


Figure 1. Interfacial defect model.

In [24,25], a method for detecting non-through defects using high voltage is described; it involves dielectric breakdown of the coating. As a result, a through defect (an air channel) is formed in the coating, which must subsequently be repaired.

It is well known that the formation of a spark discharge in a gas or a solid dielectric is preceded by a partial-discharge stage [26,27]. It also follows from [28–30] that, when a test voltage is applied to the inspected coating, partial discharges may occur within the defects described above. At the same time, these partial discharges do not lead to degradation of the coating itself. Thus, partial discharges that cause a change in the waveform of the test-voltage pulse—traditionally regarded as an interfering factor in high-voltage testing—can serve as an informative parameter, making it possible to infer the presence of interfacial defects in the coating and to estimate their geometric parameters (Figure 2).

Information on the presence of defects within the coating can be obtained either from the signal of the current-measuring element or from the characteristic change in the shape of the test-voltage pulse. However, analysis of the signal across the current-measuring shunt (Figure 3) shows that partial discharges also occur in near-surface regions of the coating, which significantly increases noise in the useful signal. Therefore, it is expedient to analyze the waveform of the test-voltage pulse.

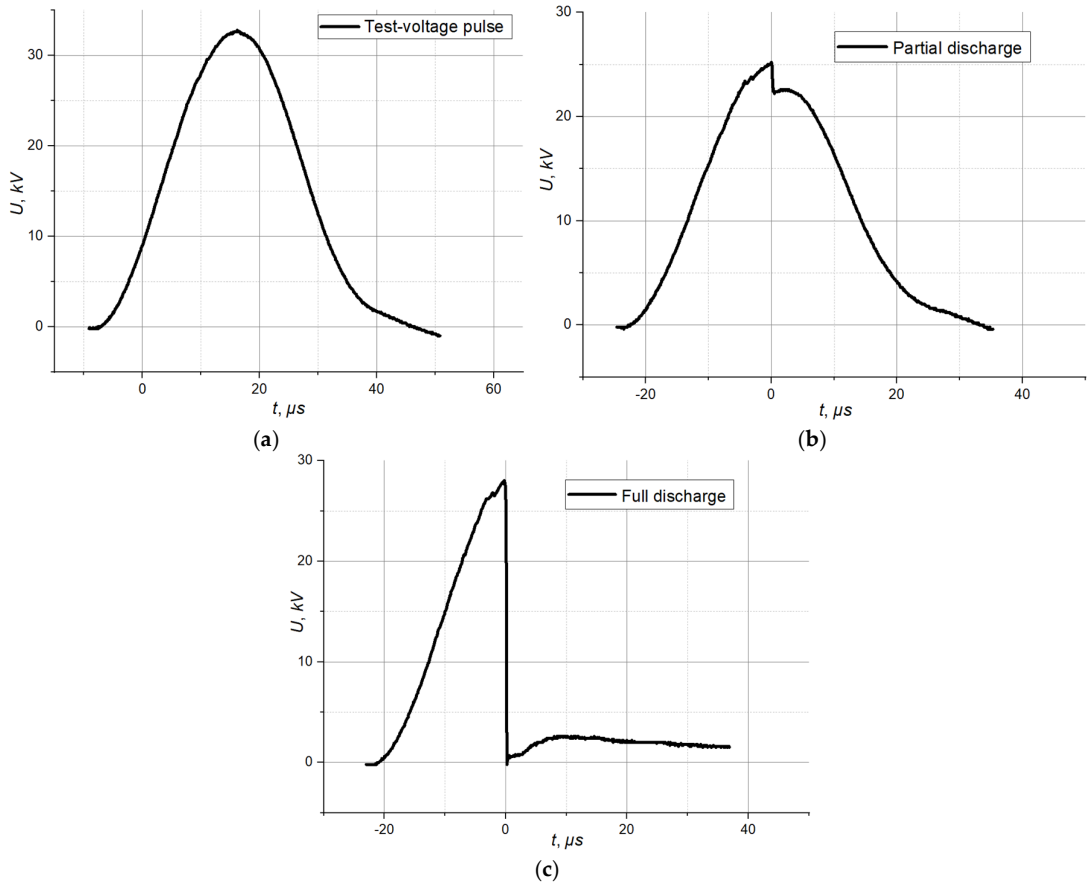


Figure 2. Test-voltage pulse waveforms: (**a**) pulse recorded on a defect-free coating area; (**b**) pulse recorded when a partial discharge occurs; (**c**) pulse recorded when a full discharge occurs on a coating area with a through defect.

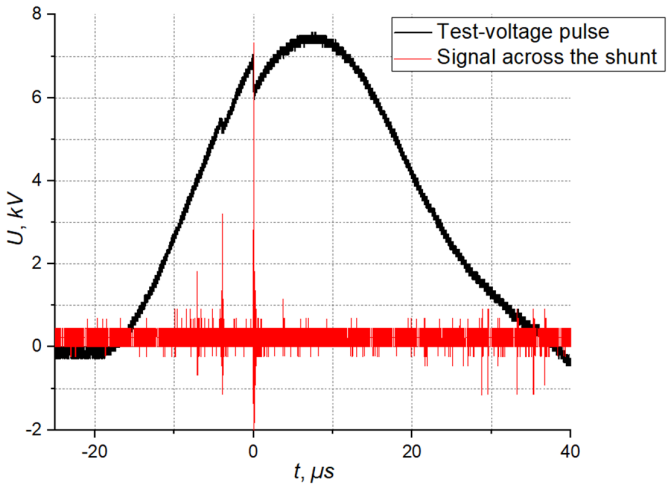


Figure 3. Test-voltage pulse of the high-voltage flaw detector with an amplitude of 17.5 kV (black) and the signal across the current-measuring shunt of the high-voltage flaw detector (red) during the occurrence of partial discharges.

In the present study, the applied voltage consisted of repetitive unipolar high-voltage pulses with a repetition rate of 50 Hz rather than sinusoidal AC voltage; therefore, conventional PRPD analysis was not applicable. The proposed method is based on time-domain analysis of pulse distortion caused by PD activity. The observed PD pulses were very short, with a characteristic frequency range of approximately 100–150 MHz.

At the same time, not every partial discharge causes a change in the charge of the electrode–coating–conductive substrate system that is sufficient to extract the partial-discharge-related signal of a non-through defect against the noise background in practical onboard implementations using embedded analog-to-digital conversion. For a quantitative description of partial discharges, a parameter known as the apparent charge is used—the charge whose instantaneous injection between the electrodes of the test object installed in the test circuit would produce the same indication on the measuring instrument as the partial-discharge pulse itself [31,32]. To model the occurrence of a partial discharge in an interfacial defect (coating delamination) filled with air, the equivalent circuit shown in Figure 4 can be employed. Modeling of gas discharges is described in [33–35].

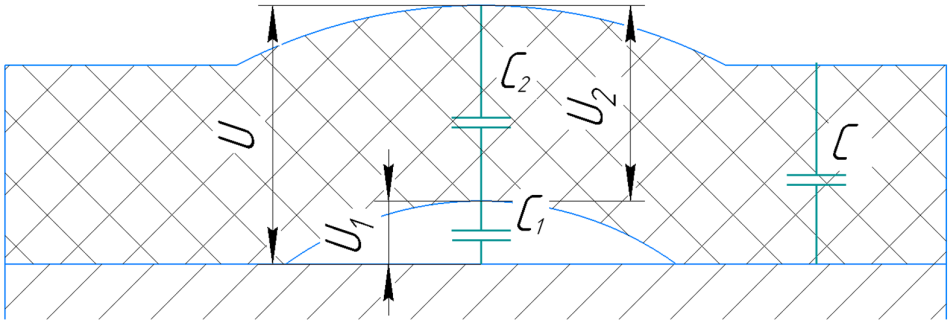


Figure 4. Equivalent circuit of a coating with an interfacial defect on a conductive substrate.

In Figure 4, U is the instantaneous applied voltage between the coating and the substrate during the high-voltage pulse; U_1 and U_2 are the voltage drops across the dielectric region at the defect location and across the air gap, respectively; C_2 and C_1 are the capacitances of the dielectric at the defect location and of the air gap, respectively. The equivalent circuit is used here as a simplified quasi-static representation of the defect region during a single pulse in order to estimate the voltage distribution and the apparent charge associated with partial discharge inception.

In addition to C_1 and C_2, the real electrode–coating–substrate system also includes a background capacitance between the high-voltage electrode and the conductive substrate through the intact coating and parasitic couplings. In the present work, this capacitance was omitted from the initial equivalent circuit only for simplicity, since the purpose of the model was to describe the local defect branch and the voltage division between the air gap and the dielectric layer at the defect location. In a more complete representation, this capacitance can be introduced as a parallel background capacitance of the electrode–coating–substrate system.

The apparent charge q of a system with an interfacial defect is calculated as follows. A fraction of the total voltage U is applied across the air gap with capacitance C_1. The voltage divides in inverse proportion to the capacitances.

$$U_1 = U \cdot \frac{C_2}{C_1 + C_2} \quad (1)$$

When the breakdown voltage U_{bd} is reached in the air cavity, a partial discharge occurs. At the instant of breakdown, the charge accumulated on the "plates" of the capacitor formed by the walls of the air gap (cavity) is neutralized. This discharge causes a redistribution of charge in the external circuit, which is recorded by the instrument as a pulse. The measured charge is equal to the apparent charge.

For capacitors C_1 and C_2 connected in series and supplied by a voltage source U, when breakdown occurs in C_1 (short-circuit model), the apparent charge q is calculated as follows:

$$q = U_1 \cdot \frac{C_2 \cdot C_1}{C_1 + C_2}, \quad (2)$$

where U_1 is the change in voltage across capacitor C_1 during the discharge.

At the instant of breakdown, U_1 drops from U_{bd} to nearly 0. Therefore, $U_1 \approx U_{bd}$.

The short-circuit representation of the air gap used here is a simplified first-order approximation. In a more general case, the voltage across the cavity after partial discharge does not necessarily drop to zero, and a residual voltage may remain after discharge. In this case, the apparent charge is lower than that predicted by the idealized model; however, the monotonic increase in apparent charge with delamination height is preserved.

For a cavity of height d_1 = 2 mm:

$$U_{bd} = E_a \cdot d_1 = 6000 \text{ V}.$$

Here, E_a = 3 kV/mm is used only as an effective first-order estimate of the air breakdown field in the simplified analytical model. In reality, the electric field inside an interfacial cavity is non-uniform and depends on the defect geometry and the permittivity of the surrounding dielectric. Therefore, the obtained analytical relationship should be interpreted as an approximate engineering estimate of the trend between apparent charge and delamination height rather than as an exact universal breakdown criterion. A more rigorous quantitative description would require a geometry-dependent correction or a local-field-based breakdown condition.

Therefore, if d_1 = 0.001 m is assumed, then:

$$q = U_1 \cdot \frac{C_2 \cdot C_1}{C_1 + C_2} = 0.21 \text{ uC}$$

Figure 5 shows the dependence of the apparent charge q on the cavity height d_1.

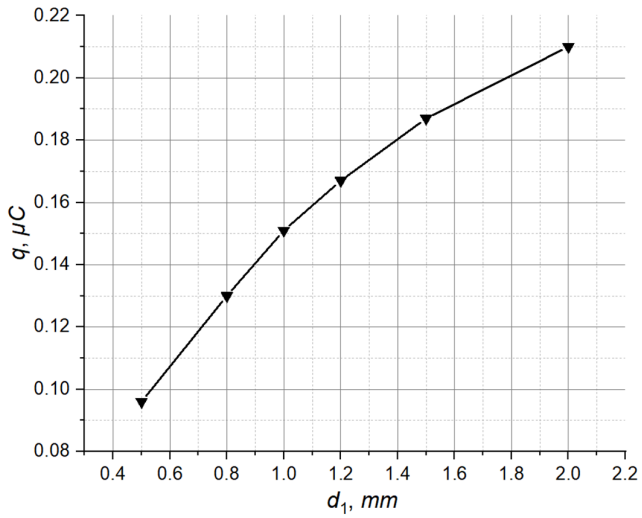


Figure 5. Dependence of the apparent charge q on the cavity height d_1.

However, as noted above, not every partial discharge can produce a change in the test-voltage pulse waveform at the electrode that is sufficient to be distinguished against the noise background. Figure 6 shows the electrode pulse waveform and the signal across the current-measuring shunt for two partial discharges as follows: in one case, the event can be reliably identified from the change in the test-voltage pulse waveform (a), whereas

in the other case it cannot (b). Figure 6 presents experimentally recorded oscillograms during partial-discharge events rather than the geometry of the coating defect itself. In the present work, spectral analysis was not performed, since the proposed method is based on time-domain detection of test-voltage pulse distortion. For each specific instrument implementation (i.e., for a given analog-to-digital converter), it is possible to determine the apparent-charge magnitude (which depends on the defect size) at which the effect of a partial discharge becomes discernible in the oscillogram of the test-voltage pulse.

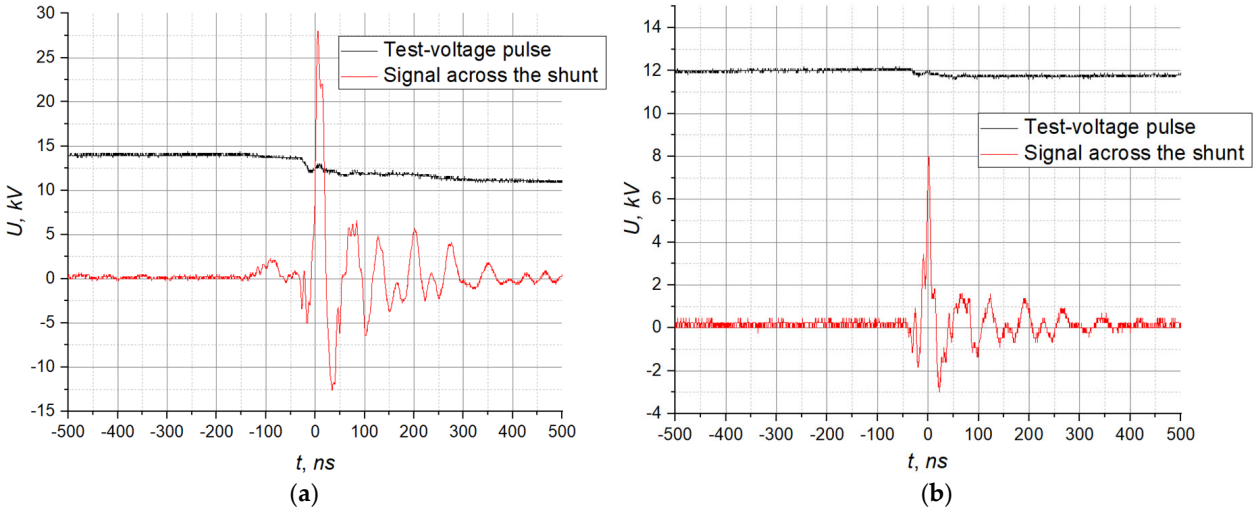


Figure 6. Oscillograms of the spark-discharge defect detector test-voltage pulse (17.5 kV amplitude, black) and the signal across the current measuring shunt during partial discharges (red): (**a**) pulse with a reliably detectable partial-discharge-induced distortion; (**b**) pulse with a partial-discharge-induced distortion that is not reliably detectable.

The calculations indicate that partial discharges associated with larger d_1 in Figure 1 are due to a higher electric charge on the boundaries of the air cavity; this, in turn, increases the partial-discharge power, making the corresponding signals easier to distinguish against external noise. This is corroborated by numerical simulations of the electric-field distribution in COMSOL Multiphysics 6.1 (Figure 7) for various coating types and thicknesses, including a 3 mm thick coating with an artificial cylindrical flat-bottom defect (air cavity). The test voltage used in the simulations was 10 kV. As the dielectric material, PMMA (Plexiglas) with a relative permittivity of $\varepsilon = 3$ was selected from the COMSOL material library.

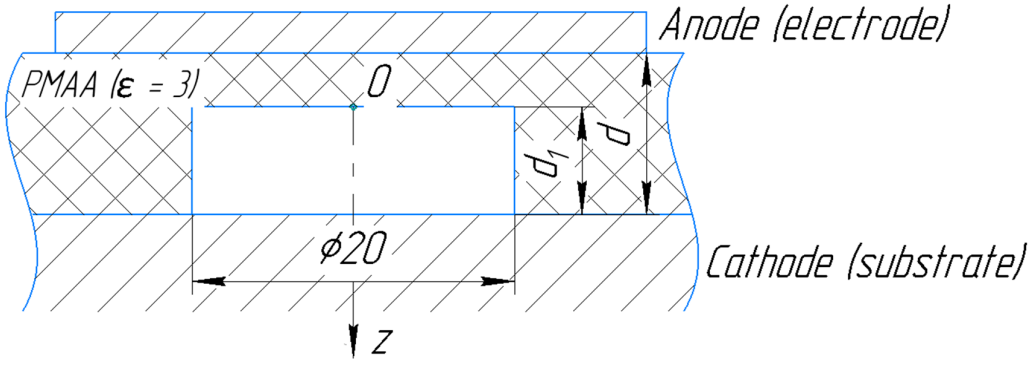


Figure 7. Model of an artificial defect in a dielectric coating used for simulating the electric-field strength distribution.

The simulation results (distribution of the electric-field strength E along the axis of the artificial defect) are shown in Figure 8.

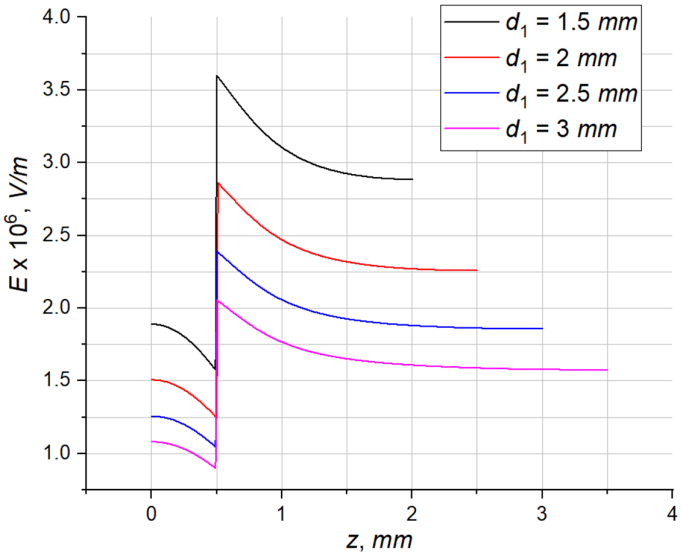


Figure 8. Distribution of the electric-field strength along the defect axis: constant dielectric thickness and variable air gap.

Figure 8 shows that, as the air gap d_1 increases, the maximum electric-field strength E in the gap also increases, which corresponds to a decrease in the effective dielectric strength of the defect region. Although this trend is physically expected, in the present work it has a specific diagnostic implication as follows: larger interfacial defects are more prone to partial-discharge inception under pulsed high-voltage testing and are therefore more likely to produce a detectable distortion of the test-voltage pulse.

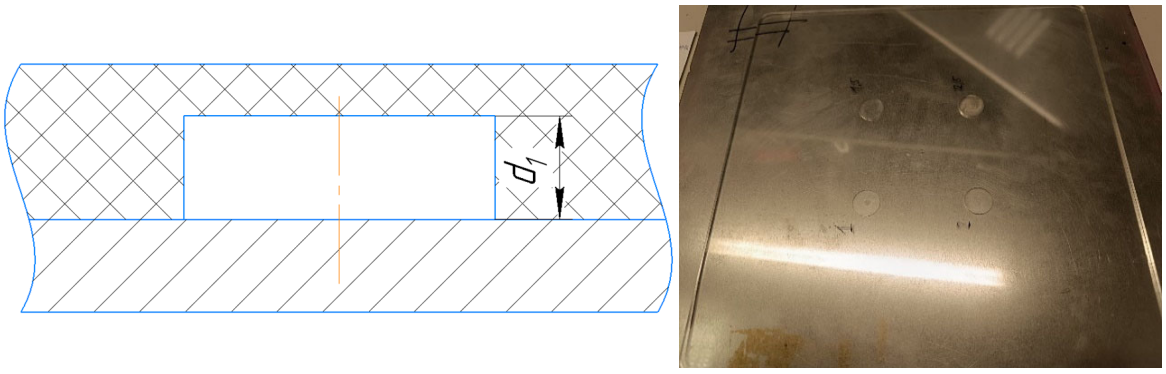
The role of the simulations is to show how the local electric-field enhancement changes with defect geometry, whereas the analytical estimate with a constant effective air strength is used only to obtain a first-order relationship between apparent charge and defect height. The final quantitative interpretation should therefore be supported by calibration for the specific coating material and defect geometry.

In the present study, PMMA (Plexiglas, $\varepsilon \approx 3$) was used as a model dielectric material in both the simulations and the experiments. The dielectric permittivity of the coating affects the capacitance ratio between the dielectric layer and the air gap and therefore influences the voltage distribution in the defect region, the local electric-field strength, and the partial-discharge inception voltage. For this reason, the approximately linear relationship between inception voltage and defect depth obtained for the Plexiglas specimens should be regarded as material-specific and should not be directly generalized to coatings with higher permittivity without recalibration.

The equivalent circuit used in the present work is a simplified first-order model intended to analyze the influence of the air-gap height for a fixed defect geometry. In reality, the lateral size of the delamination also affects the electric-field distribution because of fringing fields at the cavity edge and can therefore influence the apparent charge and the distortion of the test-voltage pulse. In the present study, the cavity diameter of the artificial defects was kept constant, while only the defect depth was varied; therefore, the reported relationships should be interpreted as valid for the investigated geometry and require recalibration for other cavity diameters.

To verify the model described above, a series of experiments were carried out in which the variation in the partial-discharge inception voltage for interfacial defects and

the possibility of extracting the partial-discharge pulse from the test-voltage pulse were analyzed. An experimental model of an interfacial defect and coating specimens with artificial defects, similar to those considered in the electric-field simulations for an interfacial defect, are shown in Figure 9. The results below correspond to experiments in which the specimens were made of Plexiglas; the spacing between adjacent blind holes was 80 mm in order to eliminate their mutual influence during the experiments. Two 5 mm thick plates were fabricated, each containing four blind holes of variable depth—from 1 to 4.5 mm in 0.5 mm increments.



(**a**) (**b**)

Figure 9. Experimental model of an interfacial defect (**a**); coating specimen with artificial interfacial defects of variable thickness (**b**).

Experimental measurements were performed using the Corona 40 Holiday Detector (NDT1 KRAFT s.r.o., Prague, Czech Republic). Signal recording was carried out with an MSO5204 oscilloscope (RIGOL Technologies Co., Ltd., Suzhou, China) with a bandwidth of 200 MHz. The following two signals were monitored during the experiments: the test-voltage pulse waveform and the signal across the current-measuring shunt. A dedicated conventional PD measuring instrument was not used in this study, since the proposed method is based on the analysis of pulse-waveform distortion caused by partial discharges in the defect region.

The oscillograms and quantitative waveform analysis presented in this paper were obtained using an MSO5204 oscilloscope. In the practical onboard implementation of the method in the Corona 40 Holiday Detector, signal processing is performed using the embedded 12-bit ADC of an STM32L4P5 microcontroller (STMicroelectronics, Geneva, Switzerland). Therefore, the detectability threshold of partial-discharge-induced pulse distortion depends on the specific electronic implementation of the instrument.

Oscillograms of the test-voltage pulse (Figure 10) were recorded using the oscilloscope trigger when the voltage exceeded a specified threshold (6.8 V, 7.2 V, 11 V, and 15 V, respectively).

The presented data demonstrate an approximately linear dependence of the partial-discharge inception voltage U_m on the blind-hole depth d_1. The scatter of the experimental points is in good agreement with the fitted straight line and remains within a 1.5% error, indicating a stable relationship. This means that, for a given total thickness of the system, the decisive factor governing the onset of partial discharges is an increase in the fraction of the air gap d_1—as d_1 increases, the effective dielectric strength of a coating containing an internal defect decreases, and discharges are initiated at a lower voltage U_m. The experimental values of the partial-discharge inception voltage as a function of blind-hole depth are summarized in Table 1.

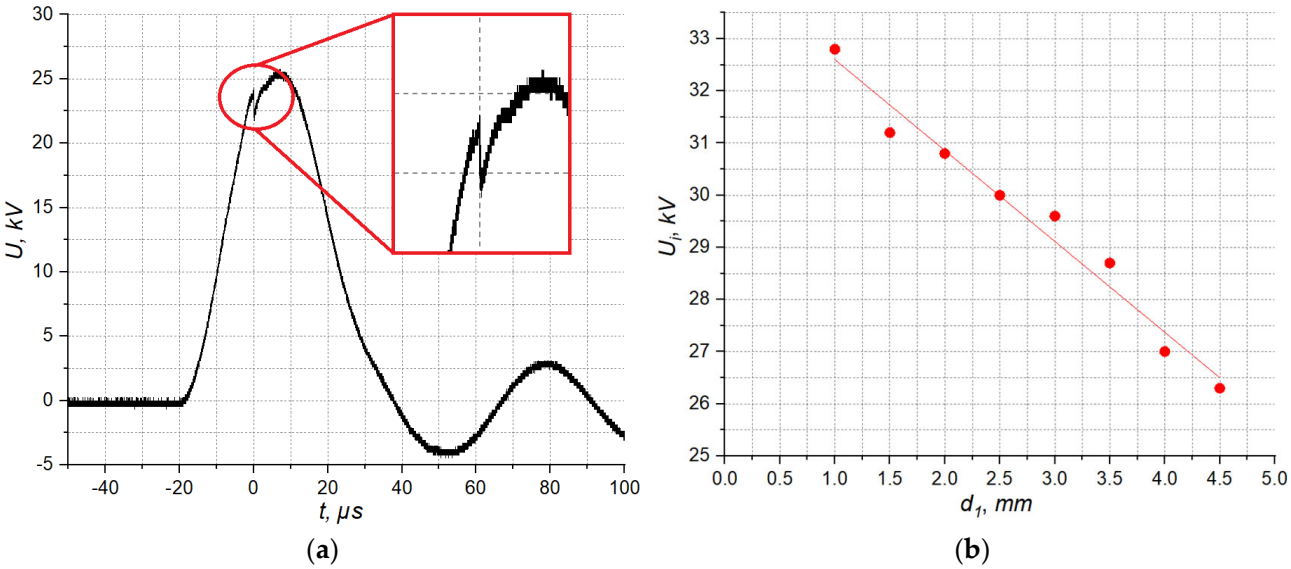


Figure 10. Test-voltage pulse showing the effect of a partial discharge as a distortion ("sag") (**a**); dependence of the partial-discharge inception voltage U_m on the depth d_1 of the blind hole (**b**).

Table 1. Partial-discharge inception voltage as a function of blind-hole depth.

d_1, mm	U_m, kV
1	32.8
1.5	31.2
2	30.8
2.5	30
3	29.6
3.5	28.7
4	27
4.5	26.3

As shown in Table 1 and Figure 10, the partial-discharge inception voltage decreases approximately linearly with increasing blind-hole depth within the investigated range.

The presented data demonstrate an approximately linear dependence of the partial-discharge inception voltage on the blind-hole depth d_1 within the investigated range. No experimental specimens with sub-millimeter defect heights were available in the present study; therefore, the observed relationship should not be extrapolated below 1 mm without additional experimental verification.

Thus, when developing an algorithm for detecting the partial-discharge signal during a ramp-up of the test voltage, information can be obtained on the presence of an interfacial defect in the coating and on the magnitude of d_1.

The authors propose an algorithm for detecting the partial-discharge signal associated with an internal defect, based on a weighted sum of increments in the root-mean-square (RMS) deviations [36,37].

Before calculating the second derivative of the test-voltage pulse, the recorded waveform was smoothed using a simple moving-average procedure over several neighboring time points in order to reduce random point-to-point noise. The averaging window was chosen empirically as the minimum smoothing required to suppress noise while preserving the characteristic pulse distortion caused by partial discharges.

To quantify deviations of the signal shape from the nominal waveform, it is expedient to use the second derivative of the test-voltage pulse:

$$\sigma_i = \sqrt{\frac{\sum(U''_i - (U''_i)_{av})^2}{n-1}}, \quad (3)$$

where σ_i is the RMS deviation of the array element i; n is the number of points in the interval under consideration; U''_i is the second derivative at the array element i; and $(U''_i)_{av}$ is the mean value of U''_i.

To determine the degree of deviation from the mean value of the second derivative of the test voltage at a given time instant, the following quantities were considered [38,39]:

$$\sigma_{iLEFT} = |\sigma_{Li} - \sigma_{Li-1}| \quad (4)$$

$$\sigma_{iRIGHT} = |\sigma_{Ri} - \sigma_{Ri+1}| \quad (5)$$

σ_{iLEFT} and σ_{iRIGHT} are the standard deviations for the measurement i over the time intervals $t \in [0, i]$ and $t \in [i, T]$, respectively, where T is the measurement duration of the test-voltage pulse consisting of $(n-1)$ points. σ_{iLEFT} views the contribution of the current measurement relative to the preceding test-voltage values and represents the evolution of the time series, whereas σ_{iRIGHT} characterizes the influence of the current measurement on the formation of subsequent test-voltage values.

To identify influential points across the entire signal, a pointwise weighted sum of the standard-deviation increments is calculated as follows:

$$W_i = \frac{t_i}{T}\sigma_{iLEFT} + \frac{T - t_i}{T}\sigma_{iRIGHT} \quad (6)$$

where $\frac{t_i}{T}$ and $\frac{T-t_i}{T}$ are weighting coefficients used to scale the obtained values.

Using an experimental example (measurements) with test-voltage pulses of 20 kV amplitude and a capacitance of 10 pF for the electrode–coating–conductive substrate system, it can be observed that full-discharge pulses are reliably identified by all the presented parameters. Next, the maximum of the array W_i is determined; its value can be used to assign the pulse to one of the classes (Figure 11). For partial-discharge identification, it is advisable to satisfy at least two classification features, since the parameters of test-voltage pulses and those of pulses containing partial discharges have a narrow separation margin.

Full-discharge pulses exhibit a distinct localization of the classification parameters that does not overlap with the other pulse types. The classification parameters of test-voltage pulses and pulses containing partial discharges are closely spaced; therefore, it is advisable to analyze all the above parameters and determine the pulse type based on the combined measurement outcome—i.e., at least two parameters must fall outside the bounds of their respective class.

The values of the classification parameters depend on the test-voltage pulse amplitude and on the capacitance of the electrode–coating–conductive substrate system. These quantities are interrelated, which makes it possible to calibrate high-voltage flaw detectors using standard specimens and to calculate threshold parameter values for specific inspection conditions.

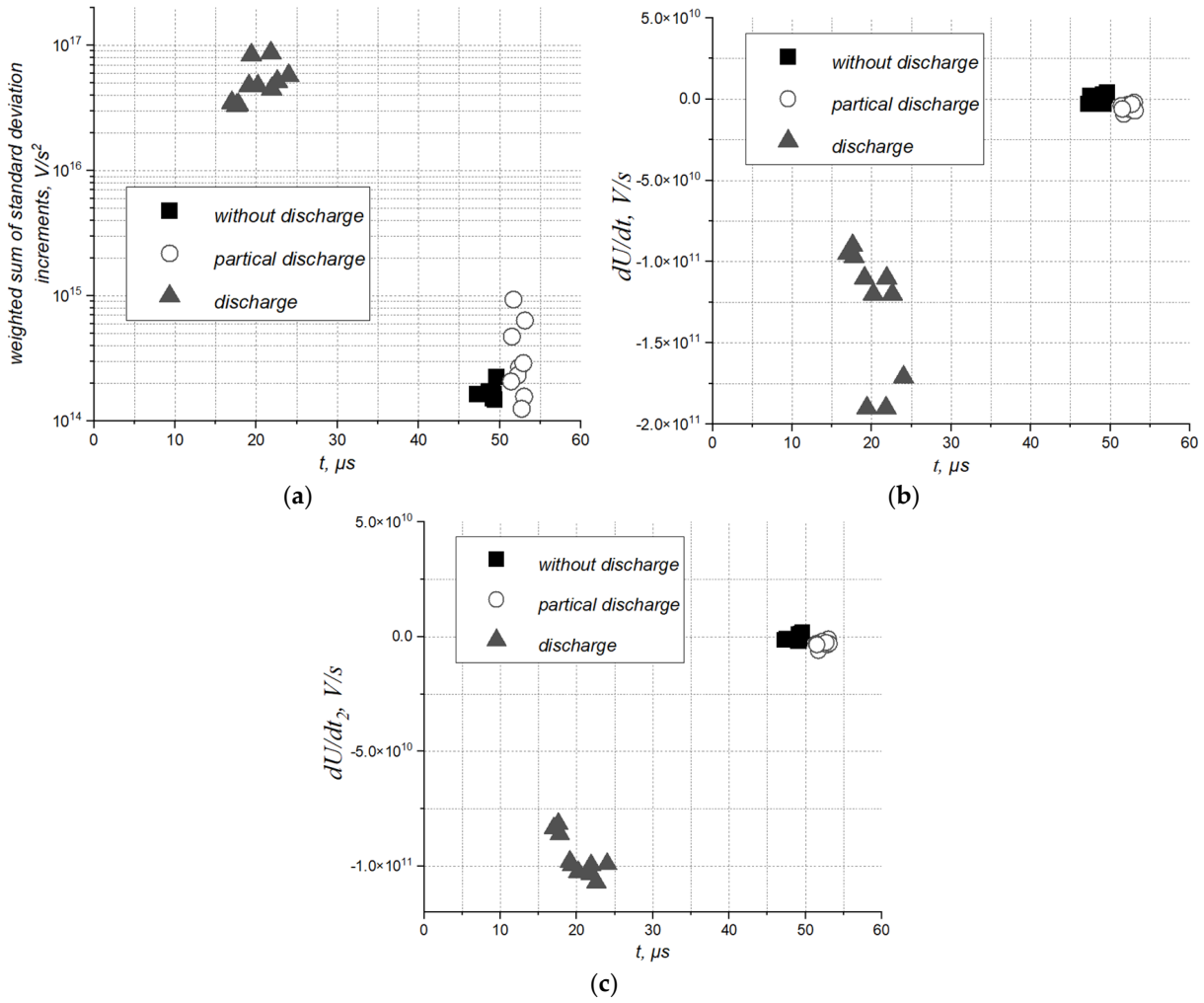


Figure 11. Distribution of classification parameters for test voltage pulses with an amplitude of 20 kV: (**a**) weighted sum of standard-deviation increments; (**b**) parameter dU/dt_1; (**c**) parameter dU/dt_2.

3. Results

Experimental validation on Plexiglas specimens with artificial interfacial defects confirmed the trends predicted by the model. Two 5 mm thick plates containing blind holes of variable depth from 1 to 4.5 mm in 0.5 mm increments were tested, with 80 mm spacing between adjacent defects. The measured values of partial-discharge inception voltage as a function of blind-hole depth are summarized in Table 1, and the corresponding dependence is shown in Figure 10b. The recorded oscillograms demonstrated that partial discharges produce a characteristic distortion ("sag") of the test-voltage pulse. The partial-discharge inception voltage exhibited an approximately linear dependence on defect depth d1, while the scatter of the experimental points remained within 1.5%, confirming the stability of the observed relationship.

Theoretical considerations, numerical simulations, and experimental results consistently show that non-through interfacial defects in dielectric coatings can be detected under pulsed high-voltage testing by using partial discharges as an informative feature. The simulations indicate that an increase in the air-gap height leads to an increase in the local electric-field strength in the defect region, which reduces the effective dielectric strength of the defect and promotes earlier partial-discharge inception. This conclusion is in agreement with the experimental results.

For the investigated model system, interfacial defects can be identified and the delamination height d_1 in the defect region can be estimated within the range 1–4 mm after calibration for the specific inspection conditions. The reported dependence should be interpreted as valid for the investigated material and defect geometry. For other coating materials, dielectric permittivities, or lateral defect dimensions, additional calibration and/or dedicated numerical simulation is required. For smaller defect heights, the detection limit was not established in the present work and may depend on the apparent-charge magnitude, signal-to-noise ratio, and specific hardware/software implementation.

The spatial resolution of the proposed approach is governed by the signal-to-noise ratio of the electrode-voltage and shunt-measurement channels, as well as by the specific hardware and software implementation of the instrument. In the present work, no experimental specimens with sub-millimeter defect heights were available; therefore, the observed relationship should not be extrapolated below 1 mm without additional verification.

Processing the parameters of the test-voltage pulse and the voltage across the current-measuring element yields a set of two-dimensional data arrays for a classifier, which can be implemented using machine-learning methods.

4. Conclusions

The feasibility of detecting non-through interfacial defects at the metal–coating interface by pulsed high-voltage testing has been demonstrated. Partial discharges arising in the defect region were shown to produce a characteristic distortion of the test-voltage pulse that can be used as an informative diagnostic feature.

The simplified equivalent-capacitive model, supported by numerical simulation and experimental validation, showed that defect geometry affects the local electric-field strength, the partial-discharge inception conditions, and the resulting pulse distortion. The experiments on Plexiglas specimens with artificial defects confirmed an approximately linear dependence of the partial-discharge inception voltage on defect depth within the investigated range.

For the investigated model system, the delamination height in the defect region can be estimated within the range 1–4 mm after calibration for the specific inspection conditions. The obtained quantitative relationships are material- and geometry-specific and require recalibration for other coating systems.

The proposed pulse-shape-based signal-processing approach provides a basis for further development of practical onboard diagnostic algorithms for high-voltage testing of dielectric coatings.

Author Contributions: Conceptualization, V.S.; Methodology, V.S. and A.M.; Software, I.G.; Validation, I.G.; Investigation, V.S.; Resources, M.S.; Data curation, V.S., A.M. and A.V.; Writing—original draft, V.S., A.M. and I.G.; Writing—review & editing, V.S., A.M., I.G., M.S. and A.V.; Visualization, I.G. and M.S.; Supervision, A.V. All authors have read and agreed to the published version of the manuscript.

Funding: This research received no external funding.

Institutional Review Board Statement: Not applicable.

Informed Consent Statement: Not applicable.

Data Availability Statement: The original contributions presented in this study are included in the article. Further inquiries can be directed to the corresponding author.

Conflicts of Interest: Author Alexey Musikhin was employed by LLC “KONSTANTA”. The remaining authors declare that the research was conducted in the absence of any commercial or financial relationships that could be construed as a potential conflict of interest.

References

1. Hellier, C.; Shakinovsky, M. *Handbook of Nondestructive Evaluation*; McGraw-Hill: Columbus, OH, USA, 2003.
2. *GOST 34395-2018*; Paint and Varnish Materials. Electrospark Method for Continuity Testing of Dielectric Coatings on Conductive Substrates. Standartinform: Moscow, Russia, 2018.
3. *AMPP (NACE) SP0188-2024*; Discontinuity (Holiday) Testing of New Protective Coatings on Conductive Substrates. AMPP: Houston, TX, USA, 2024.
4. Ibragimov, N.Y.; Ibragimova, E.N. Flaw-Detection Crack-Gauge System for Silicate Coatings of Pipes. *Defektoskopiya* **2017**, *11*, 55–57.
5. Tian, Y.; Palaev, A.; Goluntsov, A.; Liu, Z.; Shao, M.; Wang, B. Early assessment method for damage to polyethylene pipes based on linear directional waves. *Mech. Adv. Mater. Struct.* **2026**, *33*, 2456102. [CrossRef]
6. Wen, P.; Wang, X.; Tang, B.; Wang, D.; Dong, W.; Wang, L. Effect of Sealing Treatment on the Dielectric Properties of Plasma-Sprayed Al_2O_3 Coatings. *J. Therm. Spray. Technol.* **2023**, *32*, 1940–1948. [CrossRef]
7. *ASTM D5162-08*; Standard Practice for Discontinuity (Holiday) Testing of Nonconductive Protective Coating on Metallic Substrates. ASTM International: West Conshohocken, PA, USA, 2015.
8. NDT Resource Center. Spark Testing. Available online: https://www.nde-ed.org/ (accessed on 10 December 2025).
9. Kharitonova, K.A.; Kisakova, D.; Salnikova, K.E.; Molchanov, V.P. Development of methods of analysis of quality and safety posts of paint coatings. In *Modern State of Economic Systems: Economics and Management*; LLC "SFK-Office" Publisher: Tver, Russia, 2020; pp. 356–363.
10. Vasilev, E.; Gubanov, N.; Zedgenizov, D. Point defects in coated diamonds. *Diam. Relat. Mater.* **2024**, *148*, 111519. [CrossRef]
11. Afanaseva, O.V.; Tulyakov, T.F. Comparative Analysis of Image Segmentation Methods in Power Line Monitoring Systems. *Int. J. Eng. Trans. B Appl.* **2026**, *39*, 1–11.
12. Schipachev, A.; Aljadly, M.; Ganzulenko, O.; Chernikov, D.; Razzhivin, V.; Yusupov, R. Evaluating the effectiveness of magnetic-pulse treatment for healing continuity defects in the metal of oil and gas pipelines. *Metals* **2023**, *13*, 1875. [CrossRef]
13. Pryakhin, E.I.; Azarov, V.A. Study of protective properties of fluoroplastic polymer compositions on steel samples with the aim of their potential use for internal coatings of main gas pipelines. *Chernye Met.* **2025**, *4*, 62–66. [CrossRef]
14. Pham, Q.T.; Syrkov, A.G.; Silivanov, M.O.; Ngo, Q.K. Preparation of zinc nanooxide and its application for antibacterial coatings. *Tsvetnye Met.* **2023**, *9*, 51–56. [CrossRef]
15. Bolobov, V.I.; Zhukov, V.S.; Tsvetkov, A.S.; Tigranyan, G.A.; Kondratieva, V.M. Using the magnetic anisotropy method to determine the boundaries of stresscorrosion failure and prevent hydrogen damage to pipe steels. *Chernye Met.* **2025**, *2025*, 55–61. [CrossRef]
16. *ASTM G62-14*; Standard Test Methods for Holiday Detection in Pipeline Coatings. ASTM International: West Conshohocken, PA, USA, 2014.
17. *ASTM D6747-15*; Standard Guide for Selection of Techniques for Electrical Leak Location of Leaks in Geomembranes. ASTM International: West Conshohocken, PA, USA, 2015.
18. *NACE SP0188-2006*; Discontinuity (Holiday) Testing of New Protective Coatings on Conductive Substrates. NACE International: Houston, TX, USA, 2006.
19. Danikas, M.G.; Morsalin, S. Foreign Inclusions, Enclosed Cavities, Partial Discharge Models and Discharge Energy: A Short Review Regarding Solid Dielectrics and Composite Insulating Systems. *Eng. Technol. Appl. Sci. Res.* **2019**, *9*, 4659–4666. [CrossRef]
20. Mix, P.E. *Introduction to Nondestructive Testing: A Training Guide*; John Wiley & Sons: Hoboken, NJ, USA, 2005.
21. Mahdavi, F.; Forsyth, M.; Tan, M.Y.J. Techniques for testing and monitoring the cathodic disbondment of organic coatings: An overview of major obstacles and innovations. *Prog. Org. Coat.* **2017**, *105*, 163–175. [CrossRef]
22. Perdomo, J.J.; Song, I. Chemical and electrochemical conditions on steel under disbonded coatings: The effect of applied potential, solution resistivity, crevice thickness and holiday size. *Corros. Sci.* **2000**, *42*, 1389–1415. [CrossRef]
23. Varela, F.; Tan, M.Y.J.; Hinton, B.; Forsyth, M. Monitoring Cathodic Shielding and Corrosion under Disbonded Coatings. *Corros. Sci. Technol.* **2017**, *16*, 109–114.
24. Xiao, D. Fundamental theory of townsend discharge. In *Gas Discharge and Gas Insulation*; Springer: Berlin/Heidelberg, Germany, 2016; pp. 47–88.
25. Raiser, Y.P. *Physics of Gas Discharge: Study Guide*, 2nd ed.; Nauka: Moscow, Russia, 1992.
26. Varivodov, V.N.; Kovalev, D.I.; Zhulikov, S.S.; Golubev, D.V.; Romanov, V.A. Prevention of partial discharges in the solid insulation of high-voltage current conductors. *Russ. Electr. Eng.* **2021**, *8*, 30–34.
27. Starikova, N.S.; Redko, V.V. Investigation of methods for testingling the integrity of insulation in the area of weak and strong electric fields. *Bull. Sib. Med.* **2013**, *3*, 55–59.
28. Syasko, V.; Musikhin, A.; Gnivush, I. Improvement of methods and devices for multi-parameter high-voltage testing of dielectric coatings. *Coatings* **2024**, *14*, 427. [CrossRef]
29. Kuffel, E.; Zaengl, W.S.; Kuffel, J. *High Voltage Engineering Fundamentals*, 2nd ed.; Newnes (Elsevier): Oxford, UK, 2000.

30. Kreuger, F.H. *Partial Discharge Detection in High-Voltage Equipment*; Butterworths: London, UK, 1989.
31. *IEC 60270:2000*; High-Voltage Test Techniques: Partial Discharge Measurements. International Electrotechnical Commission (IEC): Geneva, Switzerland, 2000.
32. Sergeev, I.I. On Partial Discharge Measurements. *Energetik* **2016**, *9*, 41–46.
33. Sukhomlinov, V.S.; Mustafaev, A.S.; Badr, A.H.; Timofeev, N.A. Kinetic theory of the cathode sheath in low-voltage beam discharges. *Phys. Plasmas* **2025**, *32*, 113501. [CrossRef]
34. Sukhomlinov, V.S.; Mustafaev, A.S.; Badr, A.H.; Timofeev, N.A. The effect of a constant electric field in an undisturbed plasma on the stability of the electron beam-gas discharge collisional plasma system. *Phys. Plasmas* **2024**, *31*, 102111. [CrossRef]
35. Timofeev, N.A.; Sukhomlinov, V.S.; Zissis, G.; Mukharaeva, I.Y.; Mikhaylov, D.V.; Mustafaev, A.S.; Borodina, V.S. Modeling of high pressure short-arc xenon discharge with a thoriated cathode. *IEEE Trans. Plasma Sci.* **2021**, *49*, 2387–2396. [CrossRef]
36. Martínez-Tarifa, J.M.; Granado, J.; Robles, G. Efficient metrics for the detection of partial discharges under steep-fronted voltage pulses. *Int. J. Electr. Power Energy Syst.* **2022**, *141*, 108159. [CrossRef]
37. Herath, T. Field Verification of a Simple Partial Discharge Denoising Method for Generator Applications. In *IET Science, Measurement & Technology*; John Wiley & Sons: Hoboken, NJ, USA, 2020.
38. Heckert, N.A.; Filliben, J.J.; Croarkin, C.M.; Hembree, B.; Guthrie, W.F.; Tobias, P.; Prinz, J. *Handbook 151: NIST/SEMATECH e-Handbook of Statistical Methods*; NIST Pubs: Gaithersburg, MD, USA, 2002.
39. *JCGM 100:2008*; Evaluation of Measurement Data—Guide to the Expression of Uncertainty in Measurement (GUM 1995 with Minor Corrections). Joint Committee for Guides in Metrology (JCGM): Sèvres, France, 2008.

Disclaimer/Publisher's Note: The statements, opinions and data contained in all publications are solely those of the individual author(s) and contributor(s) and not of MDPI and/or the editor(s). MDPI and/or the editor(s) disclaim responsibility for any injury to people or property resulting from any ideas, methods, instructions or products referred to in the content.